Lateral Heterostructures of Multilayer GeS and SnS van der Waals Crystals

Eli Sutter,[1] Jia Wang,[1] and Peter Sutter[2,*]

[1]Department of Mechanical & Materials Engineering, University of Nebraska-Lincoln, Lincoln, Nebraska 68588, United States

[2]Department of Electrical & Computer Engineering, University of Nebraska-Lincoln, Lincoln, Nebraska 68588, United States

Abstract

Engineered heterostructures derive distinct properties from materials integration and interface formation. Two-dimensional crystals have been combined to form vertical stacks and lateral heterostuctures with covalent line interfaces. While thicker vertical stacks have been realized, lateral heterostructures from multilayer van der Waals crystals, which could bring the benefits of high-quality interfaces to bulk-like layered materials, have remained much less explored. Here we demonstrate the integration of anisotropic layered Sn and Ge monosulfides into complex heterostructures with seamless lateral interfaces and tunable vertical design using a two-step growth process. The anisotropic lattice mismatch at the lateral interfaces between GeS and SnS is relaxed *via* dislocations and interfacial alloying. Nanoscale optoelectronic measurements by cathodoluminescence spectroscopy show the characteristic light emission of joined high-quality van der Waals crystals. Spectroscopy across the lateral interface indicates valley-selective luminescence in the bulk SnS component that arises due to anisotropic electron transfer across the interface. The results demonstrate the ability to realize high-quality lateral heterostructures of multilayer van der Waals crystals for diverse applications, *e.g.*, in optoelectronics or valleytronics.

*Corresponding author: E-mail: psutter@unl.edu

Keywords: lateral heterostructures, van der Waals stacks, layered semiconductors, optoelectronics, valleytronics

Heterostructures between two-dimensional crystals promise emergent properties near interfaces between dissimilar materials.[1, 2] Vertical van der Waals heterostructures, which give rise to interlayer excitons,[3] moiré superlattice effects,[4-7] excitonic Bose-Einstein condensates,[8] *etc.*, are accessible *via* mechanical stacking of flakes exfoliated from layered crystals.[9-11] Heterostructures with covalent lateral interfaces, which enable carrier manipulation,[12] current rectification,[13-15] photodetection and light emission[16] require bottom-up synthesis since no bulk crystals exist for their isolation by exfoliation. Most lateral heterostructures so far have integrated monolayer materials such as graphene and boron nitride,[12, 17] or semiconducting transition metal dichalcogenides (TMDs).[13, 16, 18, 19] Lateral heterostructures can, in principle, also be formed from thicker multilayer van der Waals crystals, for example to achieve interfacial carrier separation or recombination in photovoltaics, photodetectors, or light emitters, or to use lateral interfaces to manipulate spin or valley polarization. However, few examples of multilayer lateral heterostructures have been reported. Among them are bilayer TMD heterostructures with improved photovoltaic performance;[20] SnS–$SnS_xSe_{(1-x)}$ core-shell structures with polarization-dependent photoresponse;[21] wrap-around SnS-SnS_2 core-shell structures showing carrier separation at type II interfaces and extended infrared response due to interfacial light absorption;[22] heterojunctions formed by thickness steps in exfoliated MoS_2;[23] and lateral multilayer VS_2 contacts to monolayer MoS_2.[24]

Here, we discuss the growth and properties of lateral heterostructures between the group IV monochalcogenides SnS and GeS, orthorhombic layered semiconductors with anisotropic optoelectronics,[25-27] optically addressable valley polarization,[28] as well as other unusual properties such as ferroelectricity.[29-31] Calculations predicted band alignments for different GeS-SnS interface orientations,[32] but heterostructures incorporating such interfaces have not been

realized to date. We synthesized high-quality GeS-SnS heterostructures and established their structure and morphology by optical microscopy, Raman spectroscopy, and (scanning) transmission electron microscopy ((S)TEM) combined with nanobeam electron diffraction. The heterostructures comprise lateral GeS-SnS interfaces with thickness-dependent alloying, as well as vertical interfaces between the SnS core and a GeS cap whose thickness is tunable *via* the growth conditions. Results from cathodoluminescence spectroscopy, used to probe the determine the optoelectronic properties across the lateral interface with nanometer resolution, are consistent with predicted band alignments and demonstrate a valley selective charge transfer and luminescence quenching near the interface, thus adding to the capabilities of interest for valleytronics.

Results and Discussion

We prepared high-quality GeS-SnS heterostructures *via* a two-step growth process (see Methods for details). First, SnS flakes were grown on mica substrates, followed by GeS growth in a separate reactor. Fig. S1 (a), (b) shows the initial SnS flakes on mica with rhombic shapes terminated by straight {110} facets; thin (< 20 nm) flakes are rounded with {110} microfacets.[33, 34] The same samples after the second (GeS) growth step show a significant increase in lateral flake size while maintaining faceted shapes (Fig. S1 (a'), (b')). For most growth conditions, they display clear optical contrast between a central region and a lateral edge band with different interference colors (Fig. S2).

Structure and morphology of flakes resulting from sequential SnS and GeS growth were investigated using (scanning) transmission electron microscopy ((S)TEM) and electron diffraction. Flakes transferred to TEM supports show faceted edges (Fig. 1 (a), (b)) and a complex morphology. Similar to optical microscopy, TEM shows a compact central region

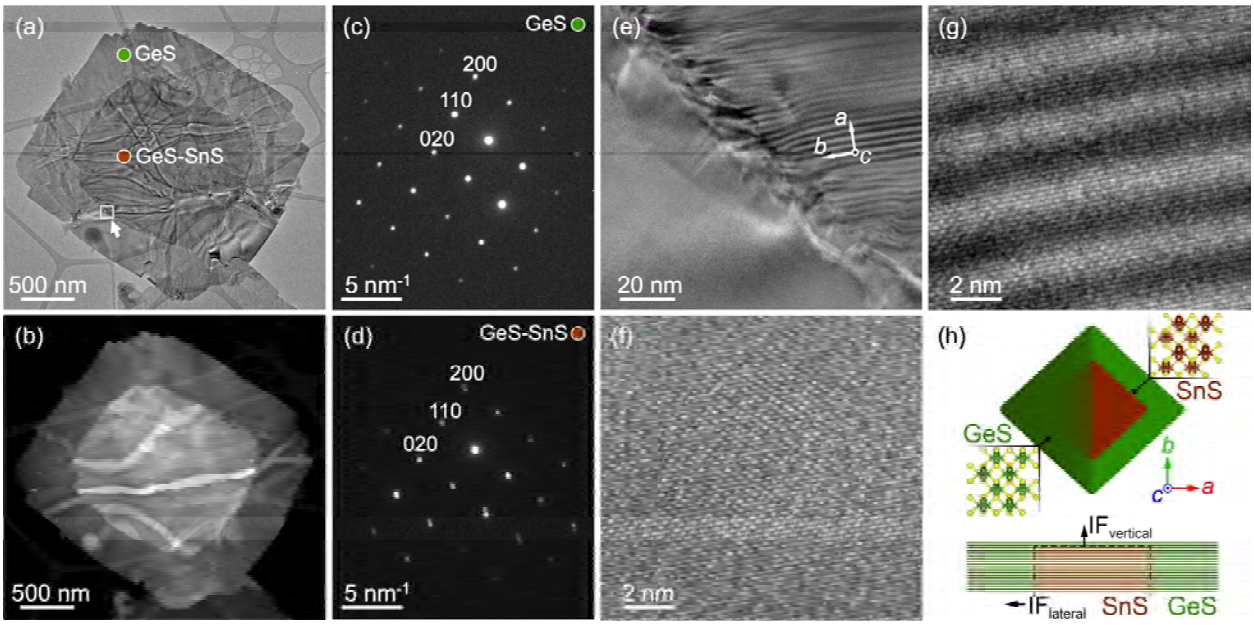

Figure 1. Morphology of GeS-SnS heterostructures. (a) TEM and **(b)** HAADF-STEM images of a characteristic GeS-SnS flake (GeS precursor temperature: 400°C). **(c)** Nanobeam electron diffraction pattern obtained in the peripheral GeS band of the heterostructure (marked in (a)); zone axis [001]. **(d)** Nanobeam electron diffraction pattern from central area of the heterostructure (marked in (a)); zone axis [001]. **(e)** HR-TEM image near the interface of the in-plane heterostructure (arrow in (a)). **(f)** High-resolution TEM of the GeS region (lower left in (e)). **(g)** High-resolution TEM of the GeS-SnS stripe moiré pattern (upper right in (e)). **(h)** Schematic top view (top) and cross-section (bottom) of the combined lateral and vertical GeS-SnS heterostructures, comprising lateral covalent ($IF_{lateral}$) and vertical van der Waals ($IF_{vertical}$) interfaces.

surrounded by a wide edge-band with different contrast. In high-angle annular dark-field (HAADF) STEM (Z-contrast imaging) the center is brighter, indicating either a higher average atomic number (Z) or greater thickness (Fig. 1 (b)). Nanobeam electron diffraction (Fig. 1 (c)) identifies the edge-band as single-crystalline GeS,[35] imaged along the [001] zone axis, while the center shows a superposition of single-crystal diffraction patterns of GeS and SnS in a vertical heterostructure with aligned lattices, stacked along [001] (Fig. 1 (d); Fig. S3).[36] GeS and SnS have identical crystal structure with anisotropic lattice mismatch. The mismatch is small along the [010] direction (*b*), with $(b_{SnS} - b_{GeS})/b_{SnS}$ = -0.27%, but substantial along [100] (*a*), where $(a_{SnS} - a_{GeS})/a_{SnS}$ = 8.9%. The large mismatch along [100] is evident in diffraction from the

central region of our heterostructures (Fig. 1 (d)), where the larger reciprocal (200) spacing corresponds to GeS. The (020) reflections coincide, consistent with the small [010] mismatch.

From the diffraction analysis, we conclude that the peripheral band is crystalline GeS whereas the center consists of a vertical GeS-SnS van der Waals stack. The presence of SnS explains the brighter HAADF-STEM contrast. High-resolution (HR) TEM (Fig. 1 (e)-(g); Fig. S4) shows the peripheral GeS seamlessly connected and lattice-aligned to the GeS-SnS center. The central GeS-SnS stack produces a stripe moiré pattern perpendicular to the *a*-direction (Fig. 1 (e), (g); Figs. S4, S5), as expected for aligned lattices with uniaxial mismatch along *a*. Sequential SnS and GeS growth thus produces heterostructures that combine both lateral and vertical interfaces between the layered crystals (Fig. 1 (h)). Note that the lateral GeS-SnS interfaces are neither armchair (parallel to *a*) nor zigzag (parallel to *b*), but are mixed {110} boundaries.[32]

Micro-Raman spectroscopy was used to further investigate the GeS-SnS heterostructures. Fig. 2 (a) shows optical contrast between center and edge-band. Growth at low GeS precursor

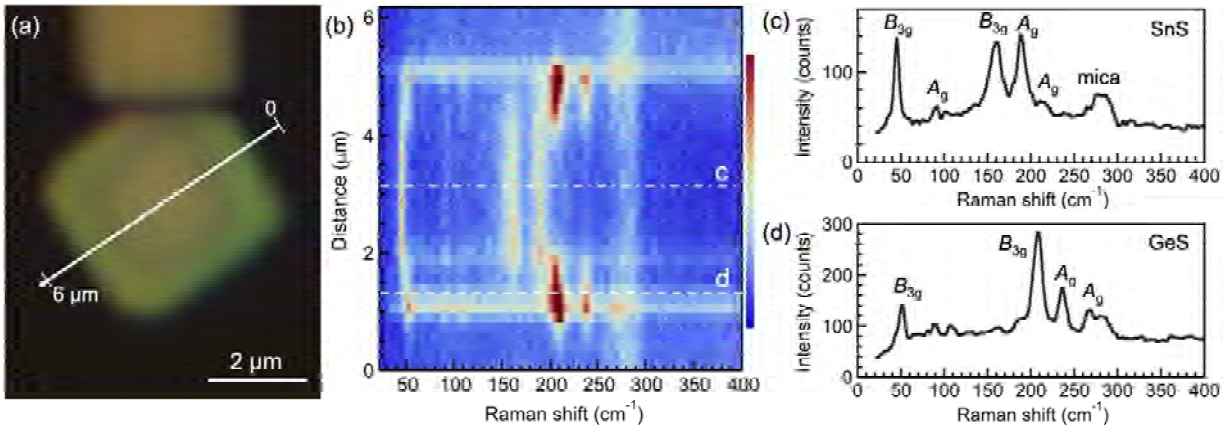

Figure 2. Raman analysis of characteristic GeS-SnS heterostructures. (a) Optical microscopy of a GeS-SnS heterostructure grown at low GeS precursor temperature (400°C). **(b)** Raman linescan across the heterostructure, as shown in (a). The false color scale is shown on the right. **(c)** Raman spectrum from the GeS-SnS center of the heterostructure (dash-dotted line in (b)), showing SnS characteristics. **(d)** Raman spectrum from the edge band (dashed line in (b)), showing GeS characteristics. Raman signal from the thin GeS overlayer across the center is not detected with the integration time used here.

temperature (400ºC) favors lateral attachment of crystalline GeS while producing ultrathin GeS top layers. Raman linescans detect only SnS modes[37] in the center (Fig. 2 (b) (c)) while the periphery shows the A_g and B_{3g} vibrational modes of GeS (Fig. 2 (d)),[38-42] consistent with the TEM results (Fig. 1; Figs. S4, S5). Note the significant redshift of the GeS modes near the interface (Fig. 2 (b)), most evident for the B_{3g} rocksalt-type mode along *a* which shifts from 210 cm^{-1} near the periphery (consistent with unstrained GeS)[42] to 205 cm^{-1} at the lateral interface to SnS. The mode softening indicates tensile strain[39, 43] or substitution of heavier Sn atoms into GeS near the interface. Additional analysis, discussed below, provides evidence for alloying at the lateral GeS-SnS interfaces.

Second-step growth at higher GeS source temperature (450ºC) produces combined lateral/vertical heterostructures with an expanded lateral GeS band and substantially increased GeS top layer thickness (Fig. S6). Top-view images show uniform flakes (Fig. S6 (a)) without the optical contrast seen in Fig. 2; Raman linescans detect only GeS modes across the entire flakes (Fig. S6 (b), (c)). Lateral heterostructures are seen in flakes stamped off the mica substrate (Fig. S6 (d)-(g); Fig. S7). Optical microscopy of the exposed flake bottom shows clear contrast between the center and periphery. For the same growth time, the edge-band is now ~4.5 μm wide, compared to ~1.2 μm at lower GeS temperature (Fig. 2). Raman linescans across the inverted flakes confirm lateral heterostructures with SnS signal in the center (Fig. S6 (f)) and GeS in the edge band (Fig. S6 (g)), consistent with TEM and electron diffraction of such flakes (Fig. S8).

The combined TEM and Raman analysis provides insight into the growth mechanisms. Following heterostructure formation, the SnS seed flakes (now encapsulated by GeS) appear intact with their {110}-faceted shape mostly preserved. This is not surprising since GeS is grown at temperatures where SnS is thermally stable.[33] Prior work showed that vapor-transport grown

SnS flakes tend to be terminated by few-layer SnS_2 due to a slight excess of sulfur in the vapor.[22] The absence of SnS_2 at our heterointerfaces implies a chemical reduction of the SnS_2 shell to SnS at the second-step growth conditions, so that pristine SnS templates the GeS growth. In heterostructures formed under identical conditions, the width of the peripheral GeS band scales with the SnS seed thickness (Fig. S9), *i.e.*, it is wider for thicker flakes and very narrow for SnS flakes with thickness below 20 nm (Figs. S4, S9, S10). This trend and our other findings discussed above were confirmed over the entire thickness range of SnS seed flakes covered here, from ~10 nm (Fig. S10) to ~200 nm. Hence, vapor-phase GeS appears to adsorb primarily on the {110} edge facets[44] due to their higher reactivity compared with the SnS and GeS basal planes and the mica surface, and the lateral GeS width can be tuned both by the SnS flake thickness and the growth conditions. The conversion of SnS seeds into SnS-GeS heterostructures by our second growth step occurs with high yield, approaching unity. Surveying over 300 heterostructure flakes by optical microscopy, we found no instance in which a SnS center was not surrounded by a lateral GeS edge band. We therefore estimate the conversion yield to be greater than $(1 - {}^{1}/_{300}) = 0.997$. Also, we did not detect any instances of 'homogeneous' nucleation of pure GeS flakes (without a SnS flake at the center), *i.e.*, the added GeS is incorporated exclusively in the edges (and to some extent on top) of the SnS seed crystals. The thin GeS top layers are likely due to the elevated reactivity of the SnS basal plane compared to other van der Waals crystals.[45] Raman linescans (Fig. 2, Fig. S10), which do not detect GeS in the center, and TEM of partially exfoliated heterostructures (Fig. S11) confirm ultrathin GeS stacked over the SnS flakes.

A distinguishing characteristic of lateral GeS-SnS heterostructures is their anisotropic in-plane lattice mismatch (as discussed above), averaging ~4% along the lateral {110} interfaces in our heterostructures. Diffraction shows unstrained SnS in the center and relaxed GeS near the

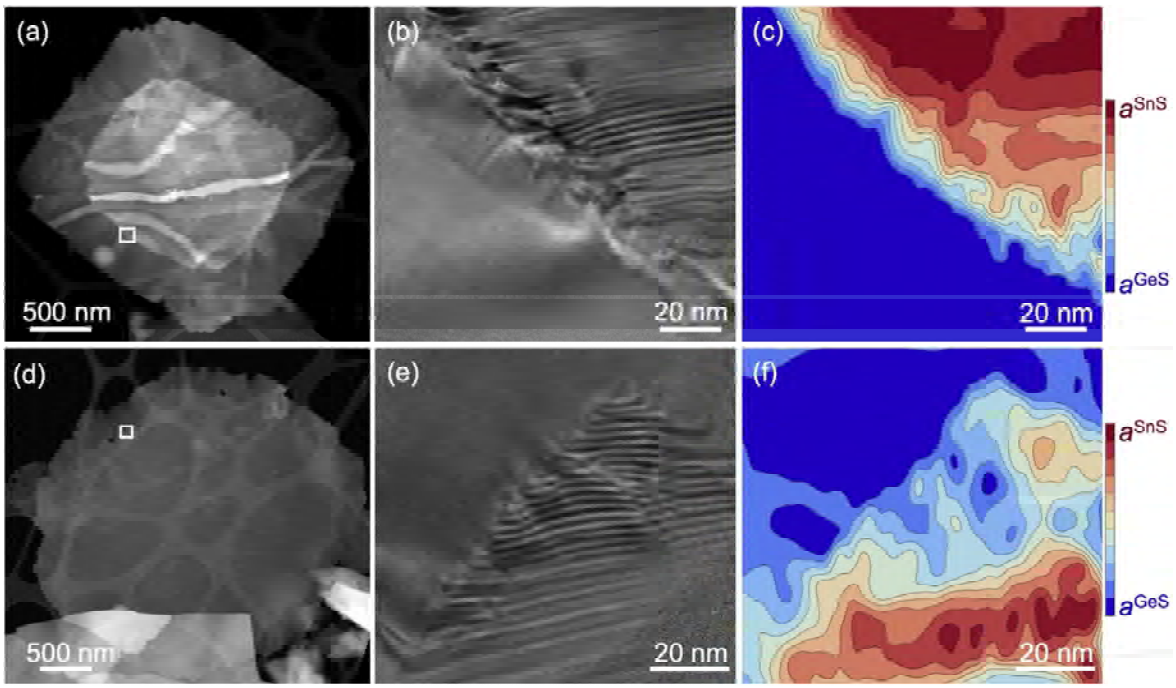

Figure 3. Analysis of [100] lattice constants across lateral GeS-SnS interfaces. (a) HAADF-STEM image of a thicker GeS-SnS heterostructure (GeS precursor temperature: 400°C). **(b)** HR-TEM image of the interfacial region (rectangle in (a)) between the GeS-SnS center (upper right, with stripe moiré) and GeS edge band (lower left, no moiré). **(c)** Fourier-analysis of the *a*-lattice constant (see Figure S13) from lattice fringes in the HR-TEM image shown in (b). **(d)** HAADF-STEM image of a thin GeS-SnS heterostructure (GeS precursor temperature: 400°C). **(e)** HR-TEM image of the interfacial region (rectangle in (d)) between the GeS-SnS center (lower right, with stripe moiré) and GeS edge band (upper left, no moiré). **(c)** Fourier-analysis of the *a*-lattice constant (see Figure S13) from lattice fringes in the HR-TEM image shown in (e).

edge (Fig. 1). Strain relaxation can involve dislocations near the interface[46] or out-of-plane ripples in the case of thin layers with sufficiently weak interaction with the substrate.[16] In addition, alloying can distribute the strain over a wider near-interface region. While HR-TEM indeed shows dislocations near the interface (Fig. S12), high-resolution images also provide evidence for interfacial alloying (Fig. 3). Given the close match between b_{GeS} and b_{SnS}, alloying is mostly reflected in changes in the *a*-lattice constant and can thus be analyzed from the *a*-values near lateral interfaces in thicker (Fig. 3 (a)-(c)) and thin (Fig. 3 (d)-(f)) heterostructures using Fourier filtering (see Fig. S13). Far from the interface, the lattice constant corresponds to a_{GeS} and a_{SnS} toward the edge and center, respectively. The transition occurs over some distance

across the interface. In thicker heterostructures, the alloy region is quite narrow (~20 nm; Fig. 3 (c), Fig. S14). Thin heterostructures show more extensive alloying (Fig. 3 (f)). Similar to lateral graphene/h-BN[17] and monolayer TMD heterostructures[47] alloying broadens lateral multilayer interfaces, here primarily *via* Sn segregation into the growing GeS as indicated by Raman linescans (Fig. 2 (b)). The thin GeS top layer invariably shows native GeS lattice constants (Fig. 1 (d)), *i.e.*, it grows after alloying has concluded.

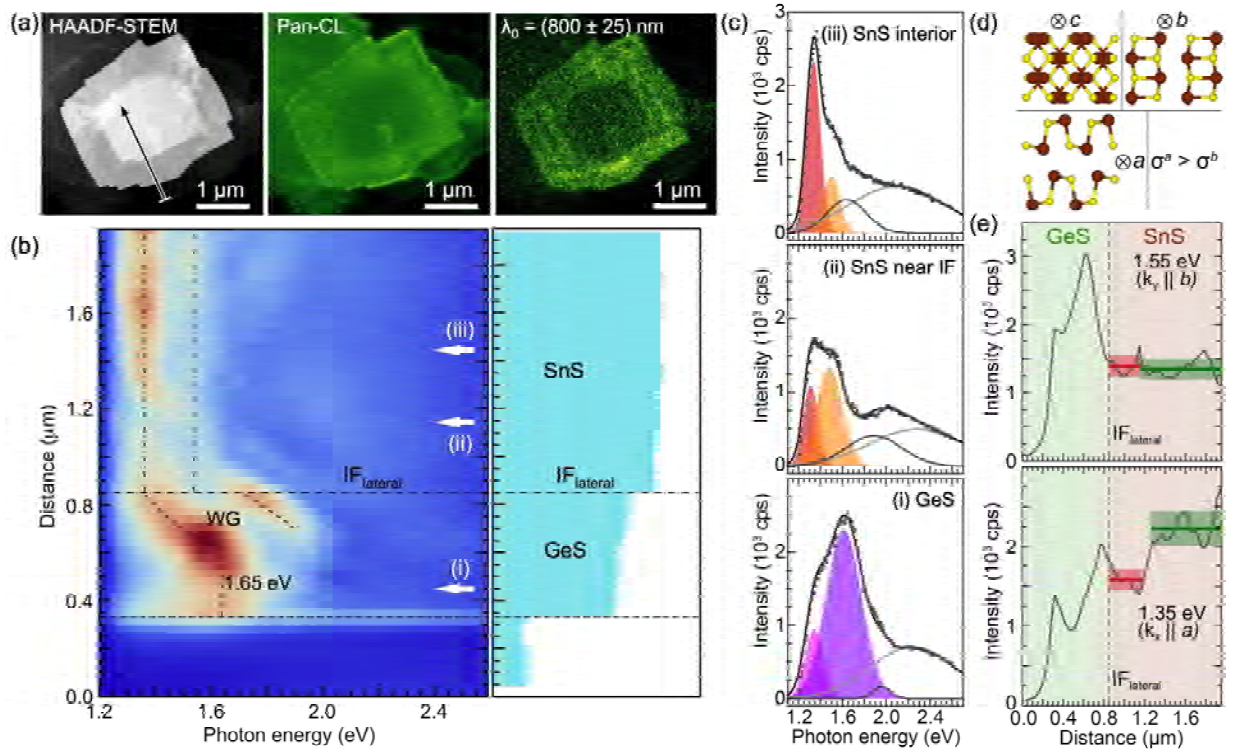

Figure 4. Nanoscale luminescence of individual GeS-SnS heterostructures. (a) (Left) HAADF-STEM image of a characteristic heterostructure; (center) Panchromatic CL map (400-1000 nm); (right) Monochromatic CL map (wavelengths: (800 ± 25) nm) of the heterostructure. **(b)** (Left) Hyperspectral STEM-CL linescan comprising full luminescence spectra along the line marked in (a). Dashed lines: GeS band-edge luminescence (photon energy: 1.65 eV) and dispersive waveguide mode interference fringes (WG). Dash-dotted lines: SnS band-edge luminescence from the *a*- and *b*-valleys. (Right) STEM intensity profile showing the positions of edges and interfaces. **(c)** CL spectra obtained at positions (i) to (iii) marked by arrows in (b). **(d)** SnS lattice structure projected along *a*, *b*, and *c* directions. The conductance is anisotropic with $\sigma^a > \sigma^b$.[48] **(e)** Luminescence intensity profiles across the lateral interface for photon energies 1.55 eV (top) and 1.35 eV (bottom), corresponding to the conduction band valleys along the *b* and *a* directions, respectively. Horizontal lines denote mean intensities near the interface and in the SnS interior. Shaded bands represent ± 1 standard deviation around the mean values.

The optoelectronic properties of GeS-SnS heterostructures were probed by cathodoluminescence spectroscopy in STEM (STEM-CL). In STEM-CL the sample is electronically excited by a focused (~1-2 nm) electron beam,[38] instead of the ~0.5 μm optical excitation used in photoluminescence spectroscopy. Hence, it allows probing the optoelectronic properties with nanometer spatial resolution near the lateral interfaces in our heterostructures. Fig. 4 (a) shows HAADF-STEM of a characteristic GeS-SnS flake, along with a panchromatic CL image and a monochromatic CL map at the bandgap energy of bulk GeS.[49] Panchromatic CL shows highest intensity at the edge, somewhat lower, nearly uniform intensity in the GeS band, and lowest emission from the SnS center. The monochromatic map clearly delineates the bright GeS edge against the dark SnS center with smaller bandgap and hence suppressed emission at this photon energy. The intensity modulation observed within the GeS band can be attributed to interference of confined photonic modes reflected by the edge facets of the heterostructure.[49]

To determine the effects of interfacial band offsets on carrier flow and recombination, we measured hyperspectral STEM-CL linescans (*i.e.*, full luminescence spectra on a linear grid) across the lateral GeS-SnS heterointerface. In interpreting the data, it is important to note that while STEM-CL involves a local excitation by a focused electron beam, recombination and photon emission (detected in the far-field) can occur a significant distance away if the carriers are displaced by drift or diffusion. The measured luminescence spectra therefore contain information on both the electronic structure at the point of recombination and possible transport of the excited carriers.

Fig. 4 (b) shows a STEM-CL linescan along the path indicated in the STEM image of Fig. 4 (a). Light emission from the GeS band closely mirrors the characteristics of pure GeS flakes, namely band-edge luminescence at 1.65 eV (Fig. 4 (c), (i)) as well as fringes due to interference

of photonic waveguide (WG) modes reflected from the edge facets (Fig. S15).[49] The situation is more complex on the SnS side of the lateral interface. Spectra in the interior are composed of two main peaks at photon energies of 1.35 eV and 1.55 eV, respectively (Fig. 4 (c), (iii)), in close agreement with the *a*- and *b*-valley bandgaps in bulk SnS.[28] Near the lateral interface to GeS, the *a*-valley emission is suppressed to less than half its intensity in the interior (Fig. 4 (c), (ii)) while the intensity of the *b*-valley peak remains constant. The luminescence quenching near the interface is further studied in Figs. 4 (d)-(e). Fig. 4 (d) illustrates the anisotropic SnS structure projected along the major crystal axes. Fig. 4 (e) shows the intensities of the two main SnS luminescence components as a function of distance from the interface. The intensity of the *b*-valley peak (1.55 eV) is constant within the experimental error. The *a*-valley peak (1.35 eV) is quenched within ~300 nm from the interface, followed by a rise to a higher, nearly constant intensity in the interior. We note that this distance is comparable to measured minority carrier diffusion lengths in single-crystalline GeS and transition metal dichalcogenides.[42, 50]

This behavior can be understood by considering the GeS-SnS band offset and the anisotropic in-plane conductivity in SnS.[48] Calculations for interfaces between relaxed GeS and SnS, as realized here, show aligned conduction band edges ($\Delta E_C \approx 0$) and valence band offsets ΔE_V = 0.45 eV along both *a* and *b* directions;[32] we assume the same situation for our mixed {110} interfaces. Electrons can thus travel without any barrier in either direction across the interface, while holes are confined to SnS. The observed *a*-valley luminescence quenching is consistent with a partial separation of electron-hole pairs in bulk SnS (facilitated by a small exciton binding energy),[51] wherein electrons diffuse into the adjacent GeS. Importantly, the anisotropic behavior with reduced near-interface intensity of the *a*-valley peak but constant *b*-valley emission indicates a valley-selective luminescence quenching. This can be explained by the different

conductivity and carrier mobility, μ, in SnS along the zigzag (*a*) and armchair (*b*) directions,[48] which favors the diffusion of *a*-valley electrons across the interface (with diffusivity given by the Einstein relation, $D = \frac{kT}{q}\mu^a$, where μ^a is the mobility along *a,* kT the thermal energy, and q the electron charge), while the *b*-valley excitations recombine radiatively within SnS. This valley-selective charge separation at interfaces between bulk GeS and SnS is distinct from the predicted electric-field induced transverse valley currents,[52] and it adds to the previously demonstrated ability of selectively exciting different valleys in bulk SnS *via* linearly polarized light.[28] Finally, the question arises why no luminescence quenching is detected on the GeS side of the interface. While further work is required to conclusively address this point, we tentatively attribute this difference to a shorter radiative lifetime in GeS limiting the effects of interfacial charge transfers.

Conclusions

Our results establish the ability to realize high-quality heterostructures of multilayer van der Waals crystals containing lateral interfaces that intersect many layers. The analysis of flakes obtained by sequential growth of SnS and GeS shows the formation of complex multilayer heterostructures in which a central SnS seed crystal is laterally integrated with a GeS edge band whose width ranges from a few hundred nm to several μm; in addition, the entire lateral heterostructure is capped by a thin GeS top layer. The orientation of the lateral interfaces follows from the {110} faceting of the SnS seeds, while the GeS top layer forms a vertical (001) van der Waals interface with the SnS center. Since for a thick multilayer heterostructure alternative strain relaxation mechanisms such as out-of-plane rippling are not available, the anisotropic lattice mismatch between GeS and SnS is accommodated by dislocation formation near the lateral interface. In addition, our analysis shows evidence for interfacial alloying, despite the fact that the miscibility of the cations – expected to be a predictor for alloying of the corresponding

chalcogenides[53] – is low in the case of Ge and Sn.[54] The creation of lateral interfaces in multilayer van der Waals heterostructures promises benefits, for example in light harvesting applications where they can support the separation of electron-hole pairs, excited by efficient light absorption in a thick layered semiconductor and transferred to a lateral interface within the plane of the covalent layers, *i.e.*, without traversing any van der Waals gaps. The particular GeS-SnS heterostructures considered here, integrating the anisotropic group IV monochalcogenides GeS and SnS, show a different type of functionality – valley-selective luminescence in SnS due to a preferential transfer of electrons from one valley across the lateral interface – and thus exemplify the broader opportunities arising with the seamless lateral integration of bulk van der Waals crystals.

Methods

Growth step I: SnS flakes on mica. SnS flakes were synthesized in a horizontal tube furnace with a single temperature-controlled zone. SnS source powder (99.99%, Sigma Aldrich) in a quartz boat was placed in the center of the heated zone. Freshly cleaved mica substrates (MTI Crystal) supported by a clean Si wafer were placed 10-12 cm from the SnS source. The reactor was pumped down to < 10^{-3} Torr by a mechanical pump, then an Ar/H_2 (ratio 98:2) carrier gas was introduced at 60 standard cubic centimeters per minute (sccm) flow rate and a pressure of 76 Torr. The temperature of the heated zone was increased to 650°C over 30 minutes and maintained at this temperature for 5 min. The reactor was then evacuated to below 10^{-3} Torr and allowed to naturally cool to room temperature.

Growth step II: Heterostructure formation with GeS. GeS was deposited *via* vapor transport from GeS powder (99.99%, Sigma Aldrich) in a separate tube furnace with two independently controlled temperature zones. The evaporation zone containing a quartz boat with GeS powder

(~25 mg) was heated to temperatures between 400-450°C, while the zone containing the pre-grown SnS flakes on mica was heated to 300°C. During growth an Ar/H_2 (ratio 98:2) carrier gas flow was maintained at 60 sccm and a pressure of 76 Torr. GeS growth was typically performed for 5 minutes, after which the samples were cooled down naturally.

Optical microscopy, Raman spectroscopy & mapping. Optical microscopy and micro-Raman spectroscopy/mapping were performed in air in a optical/Raman microscope (Horiba Xplora plus). Optical widefield imaging employed a 100× objective and image stitching using a computer controlled sample stage to cover large sample areas. For Raman spectroscopy, we used a 100× objective at 532 nm excitation wavelength, 16.8 μW laser power, and linear polarization. No analyzer was used for the scattered radiation. Spectra and linescans were measured using a 300 μm pinhole, giving ~0.5 μm spatial resolution. In total, several hundred heterostructure flakes were surveyed by optical imaging and more than 50 were analyzed in-depth by Raman spectroscopy.

Electron microscopy and nanobeam diffraction. Structure and morphology of the heterostructures were investigated by (scanning) transmission electron microscopy ((S)TEM) and nanobeam electron diffraction in an FEI Talos F200X field emission microscope. GeS-SnS flakes were transferred from mica substrates to TEM grids using stabilization by spin-coated (3000 rpm, 60 s) poly(methyl methacrylate) (PMMA) films, baked at 70°C for 5 minutes, followed by release of the heterostructure/PMMA sandwich by DI water penetration between the flakes and mica substrate.[42] After pickup by a TEM grid, the PMMA was dissolved by immersion in acetone, leaving GeS-SnS heterostructures on the grid. In some cases, the local GeS thickness was determined *via* beam current attenuation measurements, calibrated by data

obtained on GeS nanowires (see Fig. S16). Over 30 flakes examined by (S)TEM and STEM-CL (see below) showed consistent structure, morphology, and optoelectronic properties.

Cathodoluminescence spectroscopy. Cathodoluminescence spectroscopy was performed in STEM mode (STEM-CL) using a Gatan Vulcan CL holder at room temperature, 200 keV electron energy and incident beam currents of 300-600 pA. Panchromatic CL maps (512×512 pixels, 1.28 ms per pixel) were acquired by scanning the exciting electron beam across heterostructure flakes and recording the emitted light intensity across a broad wavelength range (400-1000 nm). Monochromatic maps (512×512 pixels, 2.56 ms per pixel) were acquired with a specified center wavelength (λ_0) and pass-band ($\Delta\lambda$). Hyperspectral linescans were acquired by displacing the electron beam in predefined equal steps across individual heterostructures and acquiring full CL spectra (integration time: 10 s per spectrum) at each beam position.

Acknowledgements. This work was supported by the U.S. Department of Energy, Office of Science, Basic Energy Sciences, under Award No. DE-SC0016343.

Supporting Information Available. Supporting Figures 1-16: Optical microscopy of GeS-SnS heterostructures; simulated electron diffraction patterns; additional electron microscopy of thin GeS-SnS heterostructures, of stripe moiré patterns due to vertical GeS-SnS stacking, and of heterostructures with partially exfoliated SnS centers; Raman spectroscopy and TEM of heterostructures grown at high GeS precursor temperature; dependence of GeS edge width on SnS seed thickness; dislocations near the GeS-SnS interface; analysis of the *a*-lattice parameter from high-resolution TEM; comparison of STEM-CL of GeS flakes and GeS-SnS heterostructures; GeS thickness measurement by electron beam attenuation. This material is available free of charge *via* the Internet at http://pubs.acs.org.

Author Contributions. P.S. and E.S. devised the study. J.W. carried out heterostructure growth under guidance by E.S., as well as the Raman measurements. E.S. and P.S. performed electron microscopy, nanobeam diffraction, and cathodoluminescence spectroscopy, jointly analyzed the data and wrote the paper. All authors commented on the manuscript.

Conflict of Interest. The authors declare no conflict of interest.

References

1. Geim, A. K.; Grigorieva, I. V., Van der Waals Heterostructures. *Nature* **2013,** *499*, 419-425.
2. Novoselov, K. S.; Mishchenko, A.; Carvalho, A.; Castro Neto, A. H., 2D Materials and van der Waals Heterostructures. *Science* **2016,** *353*, aac9439.
3. Rivera, P.; Yu, H.; Seyler, K. L.; Wilson, N. P.; Yao, W.; Xu, X., Interlayer Valley Excitons in Heterobilayers of Transition Metal Dichalcogenides. *Nat Nanotechnol* **2018,** *13*, 1004-1015.
4. Seyler, K. L.; Rivera, P.; Yu, H.; Wilson, N. P.; Ray, E. L.; Mandrus, D. G.; Yan, J.; Yao, W.; Xu, X., Signatures of Moiré-Trapped Valley Excitons in $MoSe_2/WSe_2$ Heterobilayers. *Nature* **2019,** *567*, 66-70.
5. Jin, C.; Regan, E. C.; Yan, A.; Iqbal Bakti Utama, M.; Wang, D.; Zhao, S.; Qin, Y.; Yang, S.; Zheng, Z.; Shi, S.; Watanabe, K.; Taniguchi, T.; Tongay, S.; Zettl, A.; Wang, F., Observation of Moiré Excitons in WSe_2/WS_2 Heterostructure Superlattices. *Nature* **2019,** *567*, 76-80.
6. Tran, K.; Moody, G.; Wu, F.; Lu, X.; Choi, J.; Kim, K.; Rai, A.; Sanchez, D. A.; Quan, J.; Singh, A.; Embley, J.; Zepeda, A.; Campbell, M.; Autry, T.; Taniguchi, T.; Watanabe, K.; Lu, N.; Banerjee, S. K.; Silverman, K. L.; Kim, S.; Tutuc, E.; Yang, L.; MacDonald, A. H.;

Li, X., Evidence for Moiré Excitons in van der Waals Heterostructures. *Nature* **2019,** *567*, 71-75.

7. Alexeev, E. M.; Ruiz-Tijerina, D. A.; Danovich, M.; Hamer, M. J.; Terry, D. J.; Nayak, P. K.; Ahn, S.; Pak, S.; Lee, J.; Sohn, J. I.; Molas, M. R.; Koperski, M.; Watanabe, K.; Taniguchi, T.; Novoselov, K. S.; Gorbachev, R. V.; Shin, H. S.; Fal'ko, V. I.; Tartakovskii, A. I., Resonantly Hybridized Excitons in Moiré Superlattices in van der Waals Heterostructures. *Nature* **2019,** *567*, 81-86.
8. Wang, Z.; Rhodes, D. A.; Watanabe, K.; Taniguchi, T.; Hone, J. C.; Shan, J.; Mak, K. F., Evidence of High-Temperature Exciton Condensation in Two-Dimensional Atomic Double Layers. *Nature* **2019,** *574*, 76-80.
9. Dean, C. R.; Young, A. F.; Meric, I.; Lee, C.; Wang, L.; Sorgenfrei, S.; Watanabe, K.; Taniguchi, T.; Kim, P.; Shepard, K. L.; Hone, J., Boron Nitride Substrates for High-Quality Graphene Electronics. *Nat Nanotechnol* **2010,** *5*, 722-726.
10. Onodera, M.; Masubuchi, S.; Moriya, R.; Machida, T., Assembly of van der Waals Heterostructures: Exfoliation, Searching, and Stacking of 2D Materials. *Jpn J Appl Phys* **2020,** *59*, 010101.
11. Frisenda, R.; Navarro-Moratalla, E.; Gant, P.; Pérez De Lara, D.; Jarillo-Herrero, P.; Gorbachev, R. V.; Castellanos-Gomez, A., Recent Progress in the Assembly of Nanodevices and van der Waals Heterostructures by Deterministic Placement of 2D Materials. *Chem Soc Rev* **2018,** *47*, 53-68.
12. Levendorf, M. P.; Kim, C.-J.; Brown, L.; Huang, P. Y.; Havener, R. W.; Muller, D. A.; Park, J., Graphene and Boron Nitride Lateral Heterostructures for Atomically Thin Circuitry. *Nature* **2012,** *488*, 627-632.

13. Duan, X.; Wang, C.; Shaw, J. C.; Cheng, R.; Chen, Y.; Li, H.; Wu, X.; Tang, Y.; Zhang, Q.; Pan, A.; Jiang, J.; Yu, R.; Huang, Y.; Duan, X., Lateral Epitaxial Growth of Two-Dimensional Layered Semiconductor Heterojunctions. *Nat Nanotechnol* **2014,** *9*, 1024–1030.

14. Sahoo, P. K.; Memaran, S.; Xin, Y.; Balicas, L.; Gutiérrez, H. R., One-Pot Growth of Two-Dimensional Lateral Heterostructures *via* Sequential Edge-Epitaxy. *Nature* **2018,** *553*, 63-67.

15. Li, M.-Y.; Shi, Y.; Cheng, C.-C.; Lu, L.-S.; Lin, Y.-C.; Tang, H.-L.; Tsai, M.-L.; Chu, C.-W.; Wei, K.-H.; He, J.-H.; Chang, W.-H.; Suenaga, K.; Li, L.-J., Epitaxial Growth of a Monolayer WSe_2-MoS_2 Lateral *p-n* Junction with an Atomically Sharp Interface. *Science* **2015,** *349*, 524-528.

16. Xie, S.; Tu, L.; Han, Y.; Huang, L.; Kang, K.; Lao, K. U.; Poddar, P.; Park, C.; Muller, D. A.; DiStasio, R. A.; Park, J., Coherent, Atomically Thin Transition-Metal Dichalcogenide Superlattices with Engineered Strain. *Science* **2018,** *359*, 1131-1136.

17. Sutter, P.; Cortes, R.; Lahiri, J.; Sutter, E., Interface Formation in Monolayer Graphene-Boron Nitride Heterostructures. *Nano Lett* **2012,** *12*, 4869-4874.

18. Gong, Y.; Lin, J.; Wang, X.; Shi, G.; Lei, S.; Lin, Z.; Zou, X.; Ye, G.; Vajtai, R.; Yakobson, B. I.; Terrones, H.; Terrones, M.; Tay, B. K.; Lou, J.; Pantelides, S. T.; Liu, Z.; Zhou, W.; Ajayan, P. M., Vertical and In-Plane Heterostructures from WS_2/MoS_2 Monolayers. *Nat Mater* **2014,** *13*, 1135–1142.

19. Zhang, Z.; Chen, P.; Duan, X.; Zang, K.; Luo, J.; Duan, X., Robust Epitaxial Growth of Two-Dimensional Heterostructures, Multiheterostructures, and Superlattices. *Science* **2017,** *357*, 788-792.

20. Sahoo, P. K.; Memaran, S.; Nugera, F. A.; Xin, Y.; Díaz Márquez, T.; Lu, Z.; Zheng, W.; Zhigadlo, N. D.; Smirnov, D.; Balicas, L.; Gutiérrez, H. R., Bilayer Lateral Heterostructures of Transition-Metal Dichalcogenides and Their Optoelectronic Response. *ACS Nano* **2019,** *13*, 12372-12384.

21. Xia, J.; Zhu, D.; Li, X.; Wang, L.; Tian, L.; Li, J.; Wang, J.; Huang, X.; Meng, X.-M., Epitaxy of Layered Orthorhombic SnS–$SnS_xSe_{(1-x)}$ Core–Shell Heterostructures with Anisotropic Photoresponse. *Adv Funct Mater* **2016,** *26*, 4673-4679.

22. Sutter, P.; Wang, J.; Sutter, E., Wrap-Around Core–Shell Heterostructures of Layered Crystals. *Adv Mater* **2019,** *31*, 1902166.

23. Tosun, M.; Fu, D.; Desai, S. B.; Ko, C.; Seuk Kang, J.; Lien, D.-H.; Najmzadeh, M.; Tongay, S.; Wu, J.; Javey, A., MoS_2 Heterojunctions by Thickness Modulation. *Sci Rep* **2015,** *5*, 10990.

24. Leong, W. S.; Ji, Q.; Mao, N.; Han, Y.; Wang, H.; Goodman, A. J.; Vignon, A.; Su, C.; Guo, Y.; Shen, P.-C.; Gao, Z.; Muller, D. A.; Tisdale, W. A.; Kong, J., Synthetic Lateral Metal-Semiconductor Heterostructures of Transition Metal Disulfides. *J Am Chem Soc* **2018,** *140*, 12354-12358.

25. Wiley, J. D.; Breitschwerdt, A.; Schonherr, E., Optical-Absorption Band Edge in Single-Crystal GeS. *Solid State Commun* **1975,** *17*, 355-359.

26. Gamzaev, D. O.; Kulibekov, A. M.; Suleimanov, R. A., Light-Exciton Mixing Effects in GeS. *Inorg Mater* **1992,** *28*, 1992-1994.

27. Wiley, J. D.; Pennington, S.; Schonherr, E., Anisotropy of the Intrinsic Photoconductivity of GeS. *Phys Status Solidi B* **1979,** *96*, K43-K46.

28. Lin, S.; Carvalho, A.; Yan, S.; Li, R.; Kim, S.; Rodin, A.; Carvalho, L.; Chan, E. M.; Wang, X.; Castro Neto, A. H.; Yao, J., Accessing Valley Degree of Freedom in Bulk Tin(II) Sulfide at Room Temperature. *Nat Commun* **2018,** *9*, 1455.
29. Fei, R.; Li, W.; Li, J.; Yang, L., Giant Piezoelectricity of Monolayer Group IV Monochalcogenides: SnSe, SnS, GeSe, and GeS. *Appl Phys Lett* **2015,** *107*, 173104.
30. Wu, M.; Zeng, X. C., Intrinsic Ferroelasticity and/or Multiferroicity in Two-Dimensional Phosphorene and Phosphorene Analogues. *Nano Lett* **2016,** *16*, 3236−3241.
31. Fei, R.; Kang, W.; Yang, L., Ferroelectricity and Phase Transitions in Monolayer Group-IV Monochalcogenides. *Phys Rev Lett* **2016,** *117*, 097601.
32. Malone, B. D.; Kaxiras, E., Quasiparticle Band Structures and Interface Physics of SnS and GeS. *Phys Rev B* **2013,** *87*, 245312.
33. Sutter, E.; Wang, J.; Sutter, P., Nanoparticle-Templated Thickness Controlled Growth, Thermal Stability, and Decomposition of Ultrathin Tin Sulfide Plates. *Chem Mater* **2019,** *31*, 2563-2570.
34. Sutter, P.; Ibragimova, R.; Komsa, H.-P.; Parkinson, B. A.; Sutter, E., Self-Organized Twist-Heterostructures *via* Aligned van der Waals Epitaxy and Solid-State Transformations. *Nat Commun* **2019,** *10*, 5528.
35. Wiedemeier, H.; Schnering, H. G. V., Refinement of the Structures of GeS, GeSe, SnS and SnSe. *Z Kristallogr* **1978,** *148*, 295-303.
36. Jain, A.; Ong, S. P.; Hautier, G.; Chen, W.; Richards, W. D.; Dacek, S.; Cholia, S.; Gunter, D.; Skinner, D.; Ceder, G.; Persson, K., Commentary: The Materials Project: A Materials Genome Approach to Accelerating Materials Innovation. *APL Mater* **2013,** *1*, 011002.

37. Sutter, P.; Wang, J.; Sutter, E., Wrap-Around Core-Shell Heterostructures of Layered Crystals. *Adv Mater* **2019,** *31*, 1902166.

38. Sutter, P.; Wimer, S.; Sutter, E., Chiral Twisted van der Waals Nanowires. *Nature* **2019,** *570*, 354–357.

39. Chandrasekhar, H. R.; Humphreys, R. G.; Cardona, M., Pressure Dependence of the Raman Spectra of the IV-VI Layer Compounds GeS and GeSe. *Phys Rev B* **1977,** *16*, 2981-2983.

40. Tan, D.; Lim, H. E.; Wang, F.; Mohamed, N. B.; Mouri, S.; Zhang, W.; Miyauchi, Y.; Ohfuchi, M.; Matsuda, K., Anisotropic Optical and Electronic Properties of Two-Dimensional Layered Germanium Sulfide. *Nano Res* **2017,** *10*, 546-555.

41. Gashimzade, F. M.; Guseinova, D. A.; Jahangirli, Z. A.; Nizametdinova, M. A., *Ab Initio* Calculation of Vibrational Spectra of Orthorhombic IV–VI Layered Crystals. *Phys Solid State* **2013,** *55*, 1802-1807.

42. Sutter, E.; Zhang, B.; Sun, M.; Sutter, P., Few-Layer to Multilayer Germanium(II) Sulfide: Synthesis, Structure, Stability, and Optoelectronics. *ACS Nano* **2019,** *13*, 9352-9362.

43. Hsueh, H. C.; Warren, M. C.; Vass, H.; Ackland, G. J.; Clark, S. J.; Crain, J., Vibrational Properties of the Layered Semiconductor Germanium Sulfide under Hydrostatic Pressure: Theory and Experiment. *Phys Rev B* **1996,** *53*, 14806-14817.

44. Sutter, E.; Sutter, P., 1D Wires of 2D Layered Materials: Germanium Sulfide Nanowires as Efficient Light Emitters. *ACS Appl Nano Mater* **2018,** *1*, 1042-1049.

45. Sutter, P.; Sutter, E., Growth Mechanisms of Anisotropic Layered Group IV Chalcogenides on van der Waals Substrates for Energy Conversion Applications. *ACS Appl Nano Mater* **2018,** *1*, 3026-3034.

46. Lu, J.; Gomes, L. C.; Nunes, R. W.; Castro Neto, A. H.; Loh, K. P., Lattice Relaxation at the Interface of Two-Dimensional Crystals: Graphene and Hexagonal Boron-Nitride. *Nano Lett* **2014,** *14*, 5133-5139.

47. Huang, C.; Wu, S.; Sanchez, A. M.; Peters, J. J. P.; Beanland, R.; Ross, J. S.; Rivera, P.; Yao, W.; Cobden, D. H.; Xu, X., Lateral Heterojunctions Within Monolayer $MoSe_2$–WSe_2 Semiconductors. *Nat Mater* **2014,** *13*, 1096-1101.

48. Tian, Z.; Guo, C.; Zhao, M.; Li, R.; Xue, J., Two-Dimensional SnS: A Phosphorene Analogue with Strong In-Plane Electronic Anisotropy. *ACS Nano* **2017,** *11*, 2219-2226.

49. Sutter, P.; Argyropoulos, C.; Sutter, E., Germanium Sulfide Nano-Optics Probed by STEM-Cathodoluminescence Spectroscopy. *Nano Lett* **2018,** *18*, 4576-4583.

50. Kim, Y. C.; Nguyen, V. T.; Lee, S.; Park, J.-Y.; Ahn, Y. H., Evaluation of Transport Parameters in MoS_2/Graphene Junction Devices Fabricated by Chemical Vapor Deposition. *ACS Appl Mater Interf* **2018,** *10*, 5771-5778.

51. Tuttle, B. R.; Alhassan, S. M.; Pantelides, S. T., Large Excitonic Effects in Group-IV Sulfide Monolayers. *Phys Rev B* **2015,** *92*, 235405.

52. Rodin, A. S.; Gomes, L. C.; Carvalho, A.; Castro Neto, A. H., Valley Physics in Tin (II) Sulfide. *Phys Rev B* **2016,** *93*, 045431.

53. Dumcenco, D. O.; Kobayashi, H.; Liu, Z.; Huang, Y.-S.; Suenaga, K., Visualization and Quantification of Transition Metal Atomic Mixing in $Mo_{1-x}W_xS_2$ Single Layers. *Nat Commun* **2013,** *4*, 1351.

54. Predel, B., Group IV Physical Chemistry, Phase Equilibria, Crystallographic and Thermodynamic Data of Binary Alloys. In *Springer Materials - Landolt-Börnstein*, Predel, B., Ed. Springer-Verlag: Berlin, Heidelberg, 2013; Vol. 12C, pp 152-153.

ToC Graphic

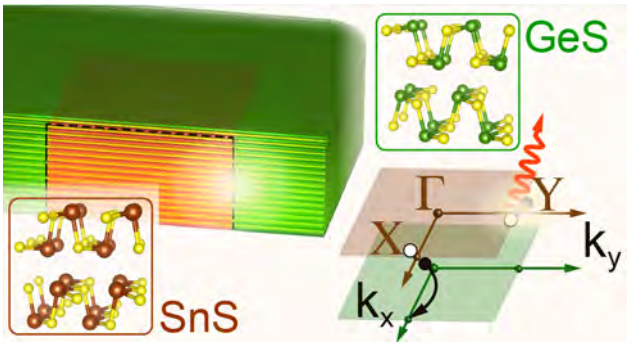

Supporting Information

Lateral Heterostructures of Multilayer GeS and SnS van der Waals Crystals

Eli Sutter,[1] Jia Wang,[1] and Peter Sutter[2,*]

[1]*Department of Mechanical and Materials Engineering, University of Nebraska-Lincoln, Lincoln, Nebraska 68588 (USA)*
[2]*Department of Electrical and Computer Engineering, University of Nebraska-Lincoln, Lincoln, Nebraska 68588 (USA)*

1. Supplementary Figures

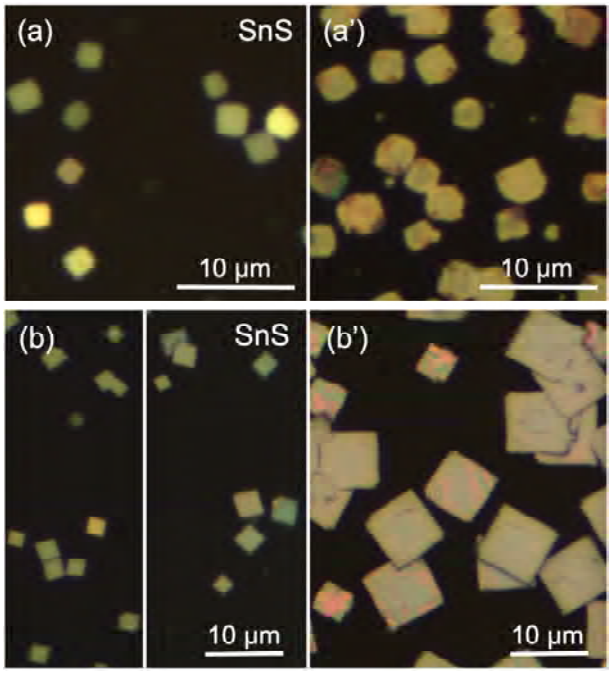

Figure S1. Morphology of SnS flakes and SnS-GeS heterostructures. (a), (b) Overview optical images of typical SnS flakes on mica substrates. **(a'), (b')** Optical images of the samples shown in (a) and (b), following additional GeS growth performed at source temperatures of 400°C and 450°C, respectively.

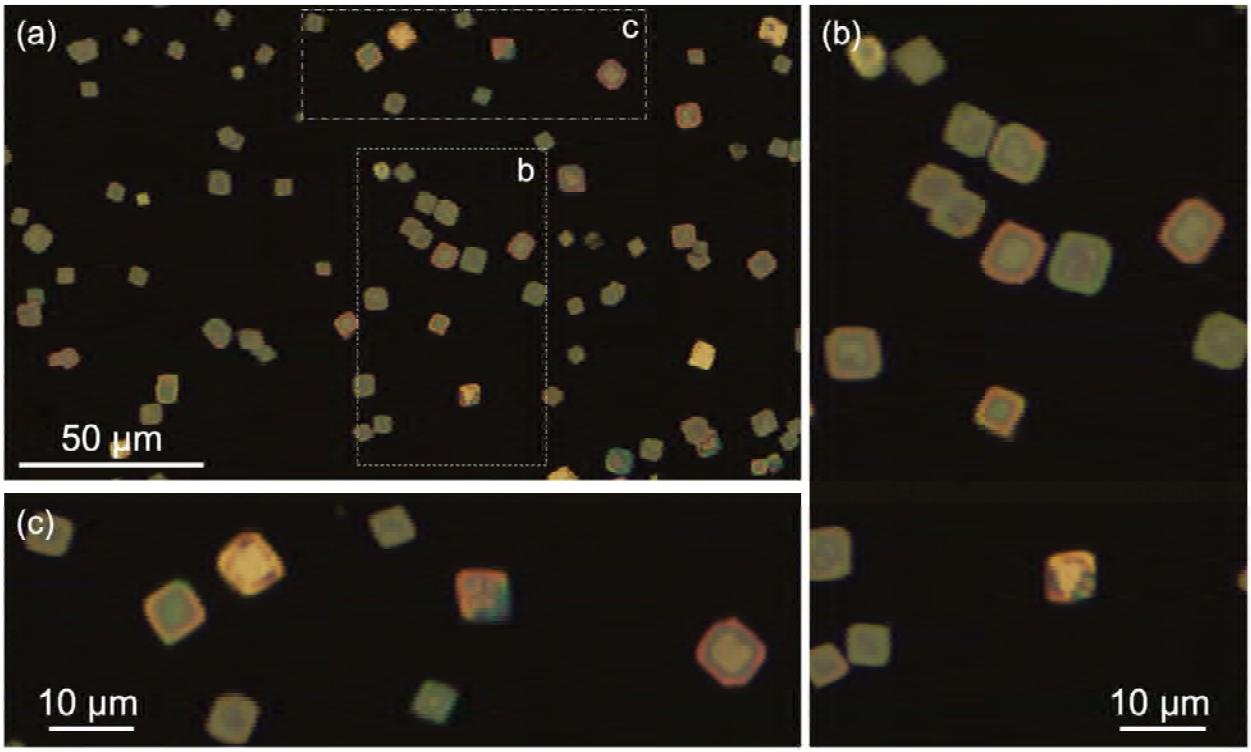

Figure S2. Heterogeneous attachment of GeS to SnS flakes, and overall yield of SnS-GeS heterostructures. (a) Overview optical image of typical SnS-GeS heterostructure flakes on mica substrate, formed with a second growth step at 320°C sample temperature and 420°C GeS source temperature. **(b), (c)** Zoomed-in optical images of the areas marked by dashed (b) and dash-dotted (c) rectangles in (a). Note the varying optical contrast due to the different flake thickness and differences between the optical constants of GeS and SnS. We find that no pure GeS flakes were (homogeneously) nucleated in the second growth step, and that each of the SnS seed flakes was converted into a heterostructure. We conclude that the areal density of heterostructures is determined by that of the SnS seed flakes, and that the yield of converting SnS seeds to SnS-GeS heterostructures is near unity.

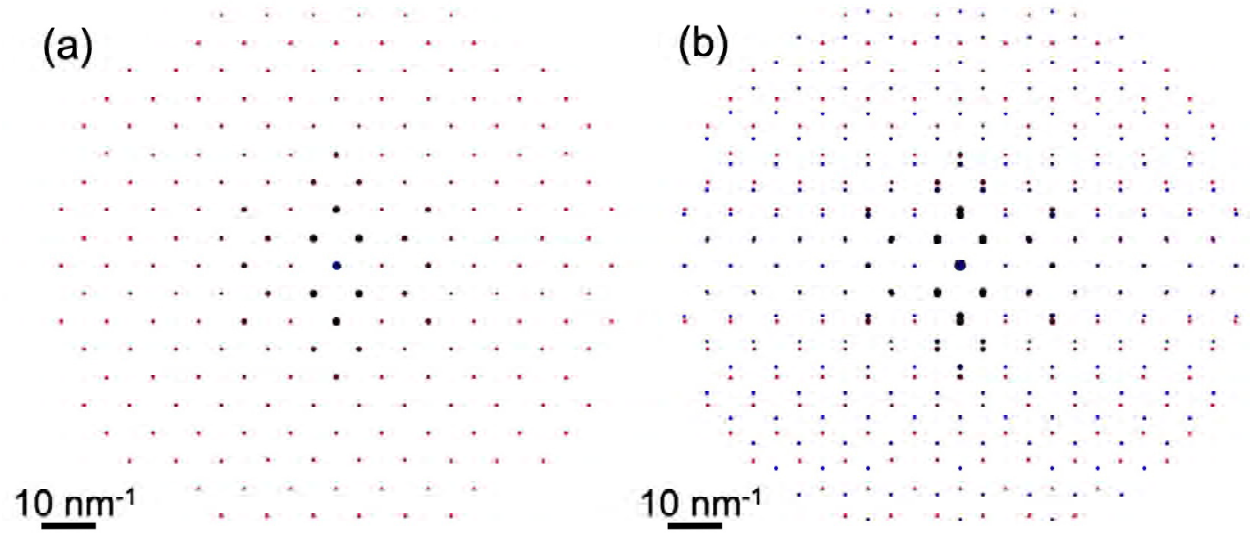

Figure S3. Simulated electron diffraction patterns along the [001] zone axis of **(a)** GeS, **(b)** superimposed GeS (red) and SnS (blue) with aligned in-plane (*a*, *b*) axes and their native (relaxed) lattice parameters.

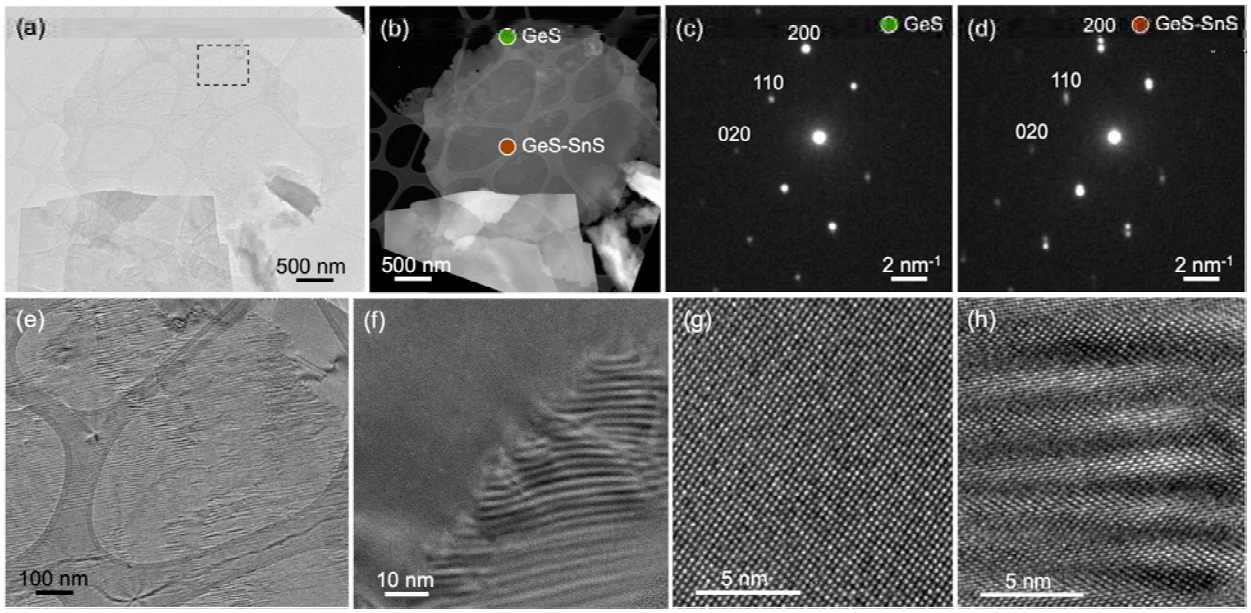

Figure S4. Morphology of thin GeS-SnS heterostructures. (a) TEM, **(b)** HAADF-STEM images of a characteristic thin GeS-SnS heterostructure (GeS source temperature: 400°C). **(c)**, **(d)** Nanobeam electron diffraction pattern from the GeS edge band and the center of the heterostructure (as marked in (b)). Zone axis: [001]. **(e)** Higher magnification TEM image of part of the flake marked by a rectangle in (a), showing a continuous moiré pattern across the central region. **(c)** Detail of the lateral interface between the GeS-SnS center (identified by the moiré**,** right) and the GeS edge (moiré-free, left). **(g)**, **(h)** High-resolution TEM images of the GeS edge and the GeS-SnS center.

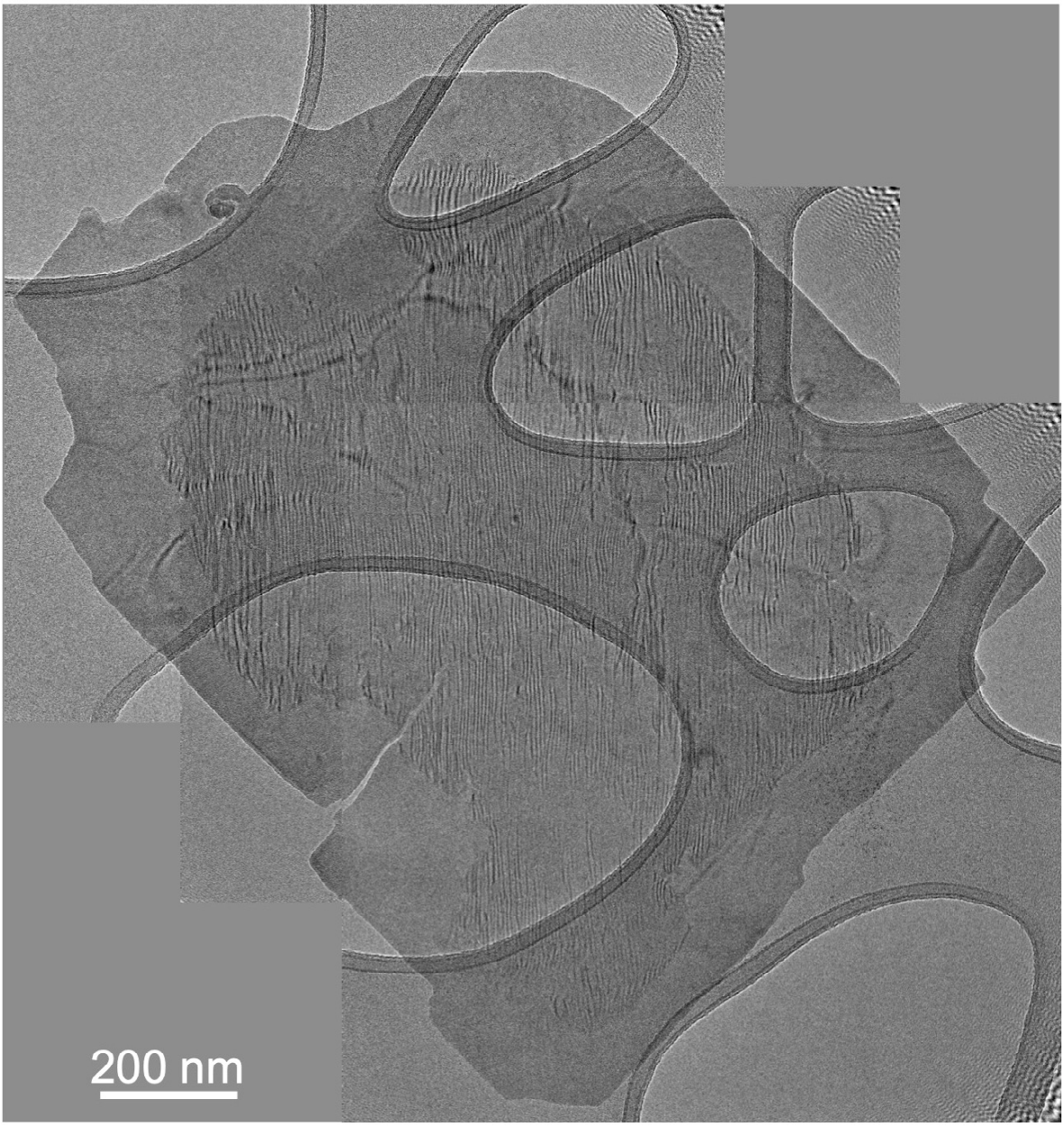

Figure S5. Stripe moiré pattern marks the extent of the central region with vertical GeS-SnS van der Waals heterostructure. Composite TEM image showing a thin GeS-SnS heterostructure. The GeS edge band is clearly distinguishable from the central GeS-SnS van der Waals stack by the presence of a stripe moiré pattern in the center and absence of the moiré near the edge.

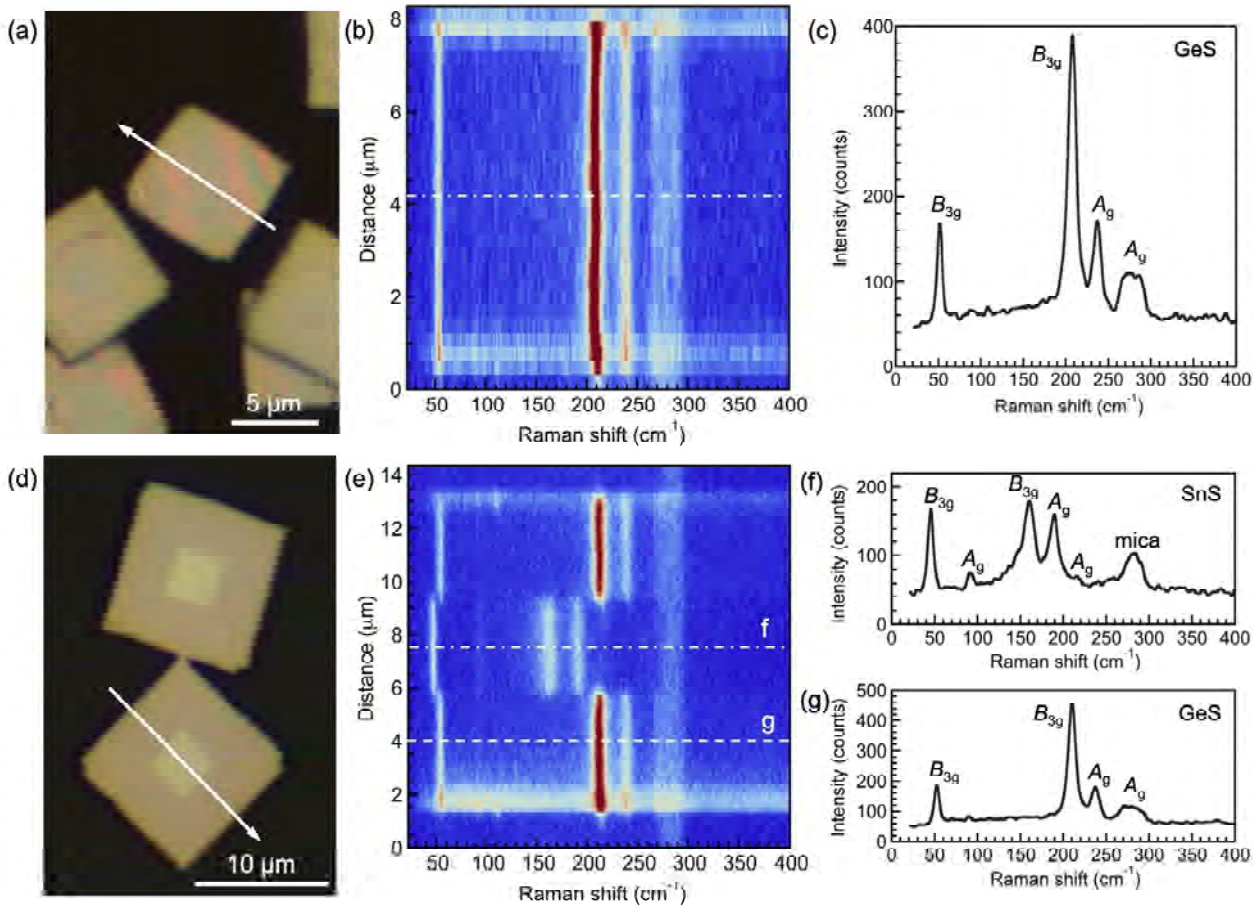

Figure S6. Raman analysis of characteristic GeS-SnS heterostructures grown from GeS precursor held at 450ºC. Measurements of the top of the heterostructures: (a) Optical microscopy of GeS-SnS flakes on the original mica substrate. **(b)** Raman linescan across one of the flakes shown in (a). **(c)** Raman spectrum showing GeS signal throughout the entire flake. **Measurements of the bottom of the heterostructures: (d)** Optical image of typical GeS-SnS heterostructures, supported by a PDMS stamp and exposing their bottom surfaces that were in contact with the mica substrate. **(e)** Raman linescan across one of the flakes shown in (d). The residual mica signal (280-290 cm^{-1}) originates from a thin layer of the van der Waals substrate that was transferred to the stamp along with the GeS-SnS flakes. **(f)**, **(g)** Raman spectra from the GeS-SnS center (dash-dotted line in (e)) and the wide GeS edge of the heterostructure (dashed line in (e)), respectively.

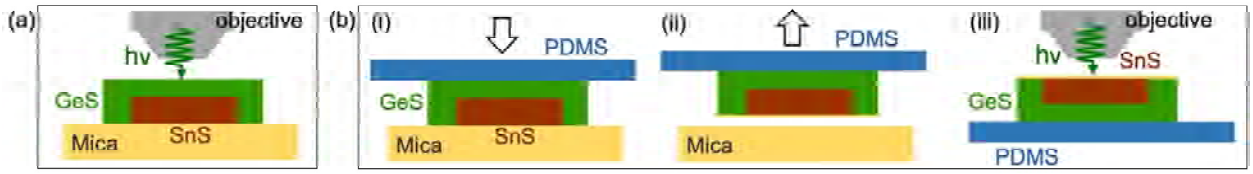

Figure S7. Schematic of the dry transfer to measure GeS-SnS heterostructures from the bottom side. (a) Conventional optical microscopy and Raman spectroscopy on the mica growth substrate. **(b)** Lift-off of heterostructure flakes using a PDMS stamp, and optical measurements from the bottom side of the flakes.

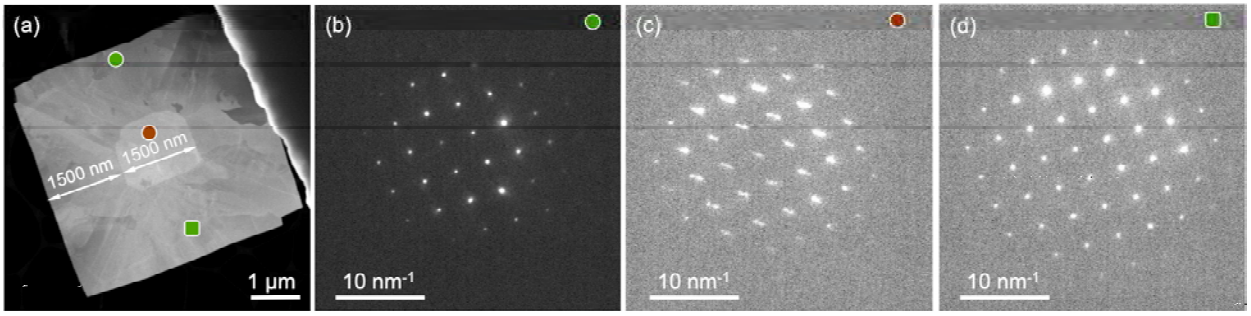

Figure S8. Morphology of GeS-SnS heterostructure grown from GeS precursor held at 450ºC. (a) HAADF-STEM image of a characteristic GeS-SnS flake, similar to the flakes shown in Figure S4. **(b)-(d)** Nanobeam electron diffraction patterns at different positions of the heterostructure, as marked in (a).

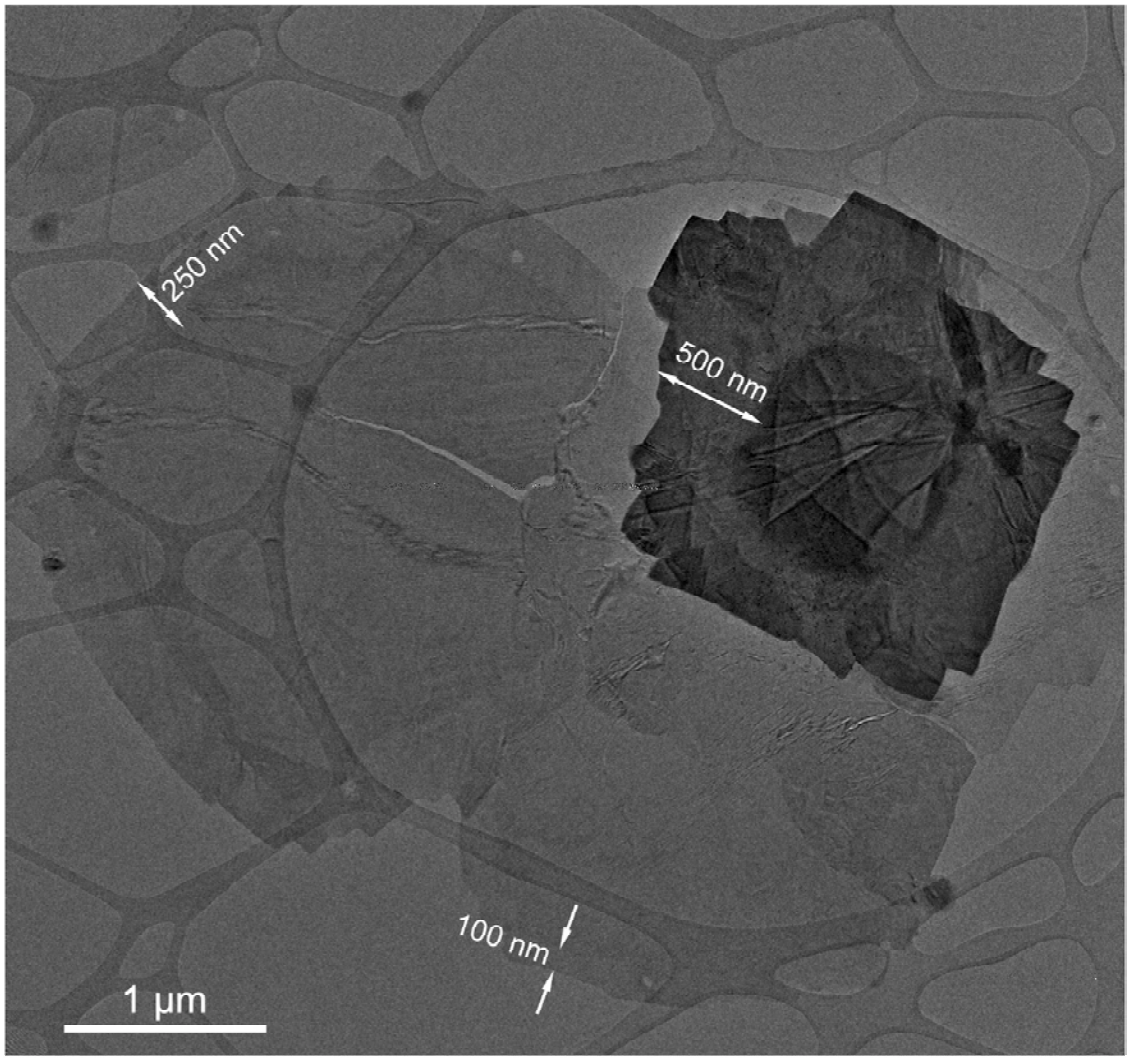

Figure S9. GeS edge width in GeS-SnS heterostructures with different thickness. TEM image comparing three characteristic GeS-SnS heterostructures with different thickness of the original SnS flakes, grown under the same conditions (GeS source temperature: 400ºC). The GeS edge width decreases with decreasing SnS flake thickness.

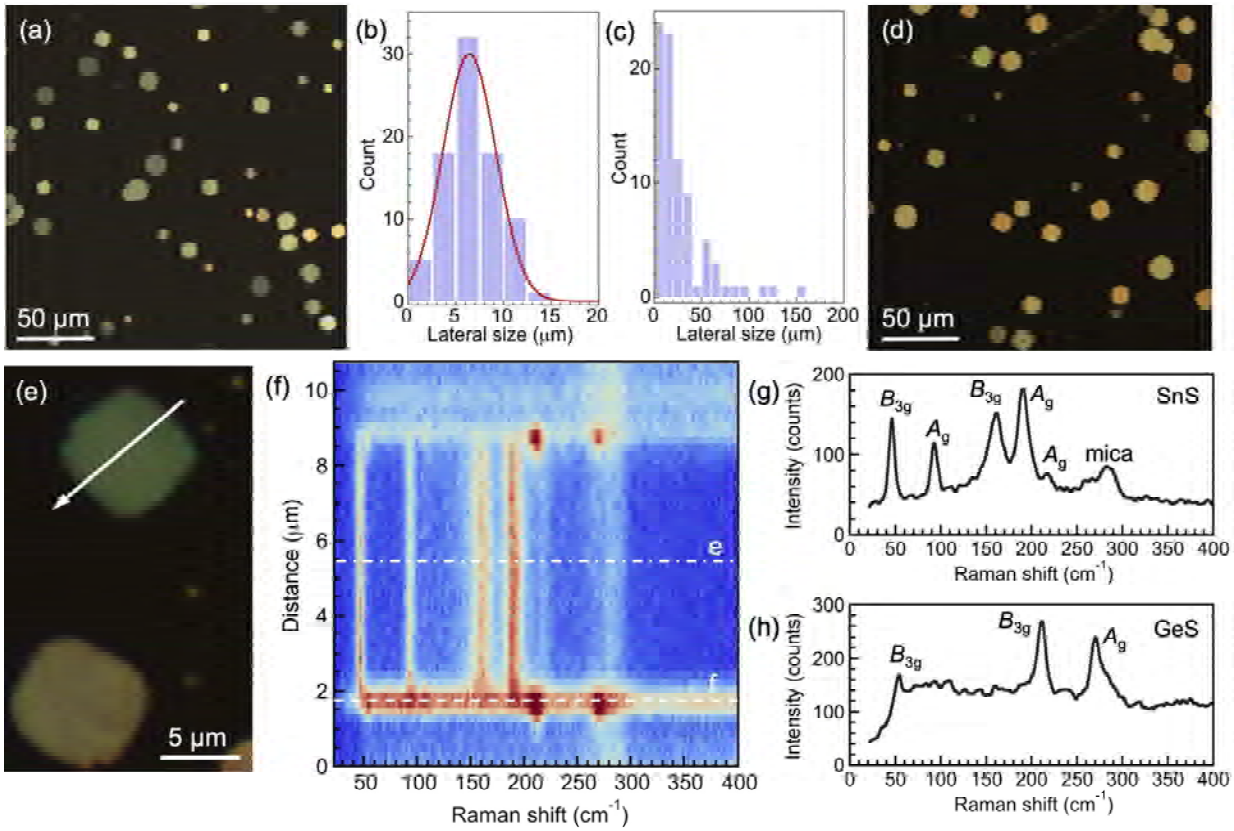

Figure S10. GeS-SnS heterostructures formed from thin SnS flakes. (a) Optical microscopy image of thin SnS flakes on mica substrate. Note the characteristic microfaceted, rounded (rather than rhombic) shape observed for thin SnS flakes. **(b)** Histogram of lateral sizes of the thin SnS flakes, obtained from AFM measurements. Red line: Gaussian fit showing a mean lateral size of 6.4 μm. **(c)** Thickness histogram of the thin SnS flakes, obtained from AFM measurements. Note the pronounced peak at thickness below 50 nm. **(d)** Image of a different region of the same sample following GeS growth. **(e)** Higher magnification optical image of a characteristic GeS-SnS heterostructure. **(f)** Raman linescan across one of the flakes shown in (c). **(g)**, **(h)** Raman spectra from the GeS-SnS center of the heterostructure and the narrow GeS edge, respectively.

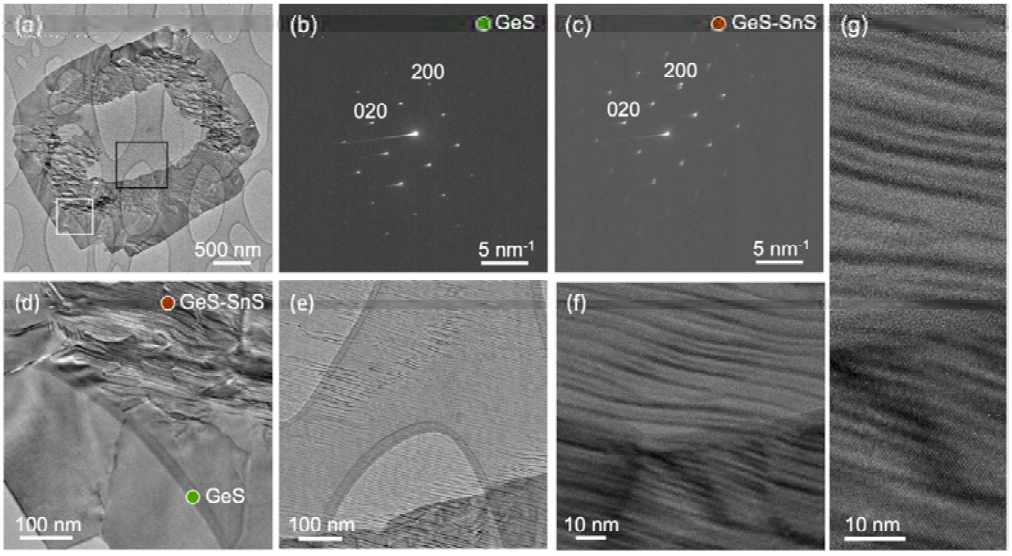

Figure S11. Morphology of a GeS-SnS heterostructure in which part of the SnS center has been exfoliated during transfer to a TEM support. (a) TEM image of a characteristic GeS-SnS flake with partially removed central region. **(b)** Electron diffraction pattern from the GeS edge. Zone axis: [001]. **(c)** Nanobeam electron diffraction from the center of the flake showing the superposition of the GeS and SnS reflections after the thinning of the SnS in the center. **(d)** Higher magnification TEM image of the interface between the GeS edge and the moiré superlattice in the GeS-SnS center (white rectangle in (a)). **(e)** TEM image showing moiré fringes in the area where part of the SnS was removed (black rectangle in (a)). While the persistent moiré pattern demonstrates stacked GeS-SnS, the lighter contrast of the center compared to the GeS edge clearly shows that vertically grown GeS layer is much thinner that the laterally grown GeS of the edge. **(f)**, **(g)** High-resolution TEM images of the moiré fringes in the center of the heterostructure.

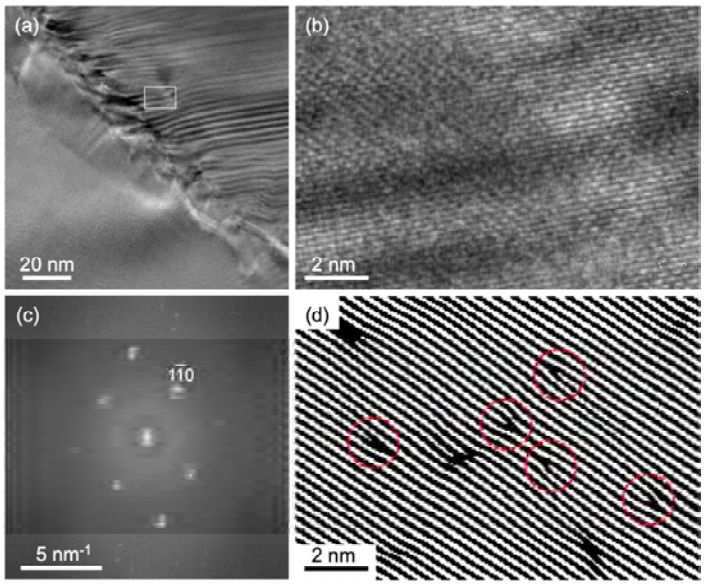

Figure S12. Dislocations near the lateral GeS-SnS interface. (a) HRTEM image obtained near the lateral interface of a GeS-SnS heterostructure. **(b)** Magnified view of the area marked by a rectangle in (a). **(c)** FFT power spectrum of the HRTEM image shown in (a). **(d)** Image (b), Fourier-filtered with portion of the $1\bar{1}0$ spot marked in (c). Red circles indicate edge dislocations in the image.

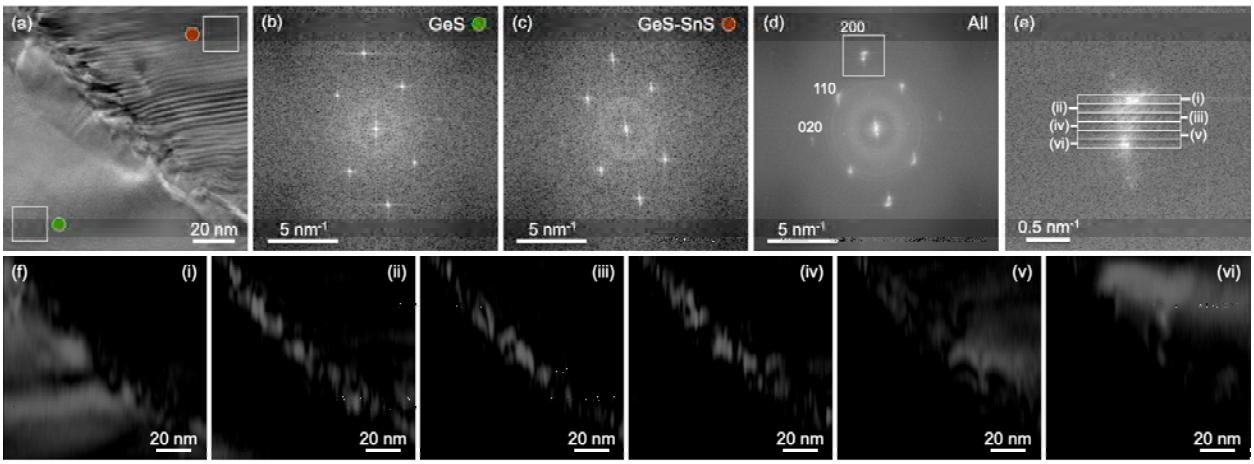

Figure S13. Fast-Fourier transform (FFT) analysis of *a*-lattice constants from HRTEM near the interface. (a) HRTEM image obtained near the interface of a GeS-SnS heterostructure. Moiré free parts (lower left) correspond to the GeS edge; regions with stripe moiré mark the GeS-SnS vertical heterostructure. **(b)** FFT power spectrum from the lower left rectangle in (a), showing GeS reciprocal spots. **(c)** Power spectrum from the upper right rectangle in (a), showing relaxed GeS and SnS. **(d)** FFT power spectrum of the entire area shown in (a). **(e)** Detail of the (100) spot, with marked rectangular areas ((i) through (vi)) from which inverse-FFT images were obtained. Region (i) corresponds to a^{GeS}, while region (vi) corresponds to a^{SnS}. **(f)** Fourier-filtered images from reciprocal space regions (i) through (vi) marked in (e).

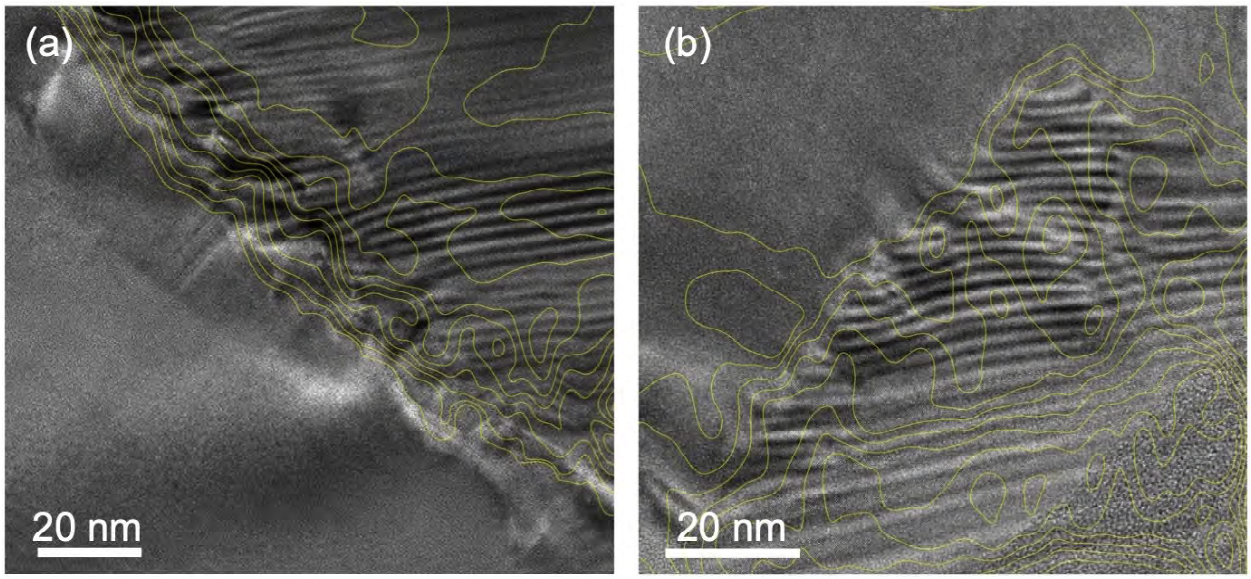

Figure S14. Alloyed region and stripe moiré pattern at the lateral interface. (a) HRTEM image and contours of the gradually changing *a* lattice constant across the interface for the thick heterostructure shown in Figure 3 (a)-(c). **(b)** HRTEM image and contours of the gradually changing *a* lattice constant across the interface for the thin heterostructure shown in Figure 3 (d)-(f).

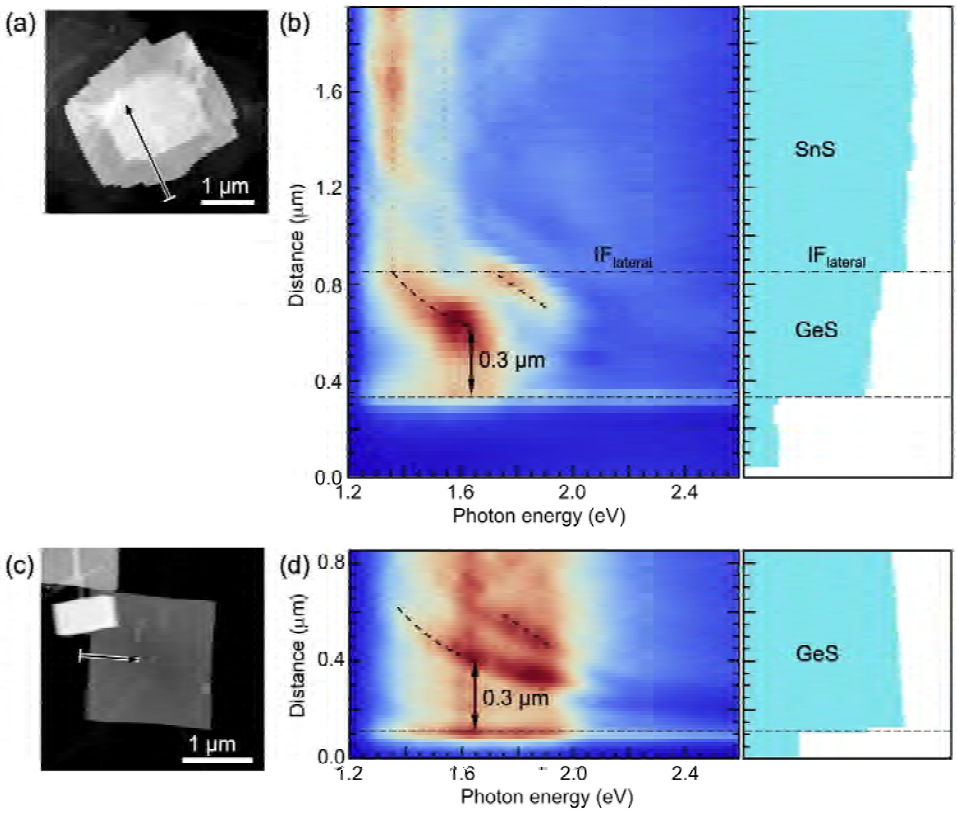

Figure S15. Waveguide mode interference in GeS-SnS heterostructures and GeS flakes. (a) HAADF-STEM image of the GeS-SnS heterostructure shown in Figure 4. **(b)** (Left) Hyperspectral STEM-CL linescan along the arrow shown in (a); (right) corresponding STEM intensity, showing the position of the flake edge and lateral GeS-SnS interface ($IF_{lateral}$). **(c)** HAADF-STEM image of a pure GeS flake. **(d)** (Left) Hyperspectral STEM-CL linescan along the arrow shown in (c); (right) corresponding STEM intensity, showing the position of the flake edge. Dashed lines in (d) mark the dispersion of fringes due to constructive interference of the primary luminescence with waveguide modes reflected from the flake edge. While there are differences in the intensity distribution, the same dispersive fringes are found in the GeS edge band of the GeS-SnS heterostructure.

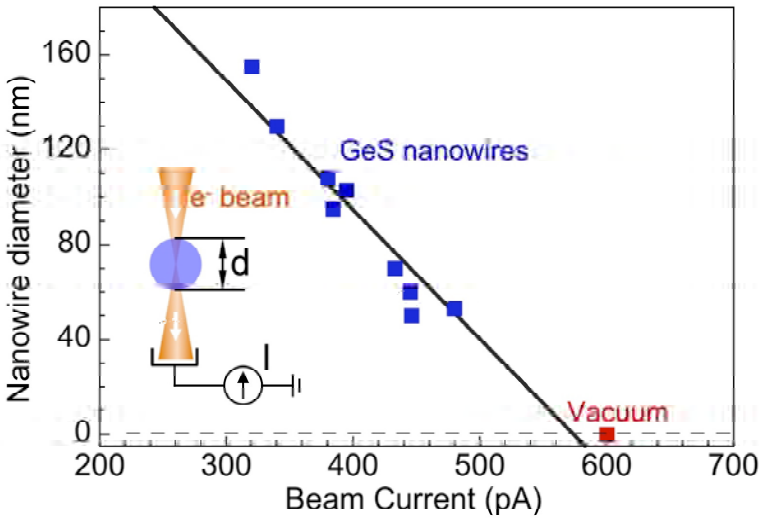

Figure S16. Determining the (vertical) thickness of the GeS edge band from electron beam current attenuation. Measurements of the electron beam current on suspended GeS nanowires with different diameters (d, blue symbols) in comparison with the beam current measured in vacuum (without a sample, red symbol), used to calibrate the attenuation of the electron beam current as a function of GeS thickness. The inset shows a schematic of the measurement, in which the electron beam after traversing the sample is collected by a Faraday cup and its current (I) measured by a pico-ampere meter.